

our "dry" calculation, we zeroed out the radiative effects of water vapor but still used the moist adiabat for the tropospheric temperature profile. This corresponds to the typical practice in radiative-convective modeling of using the moist adiabat even in highly subsaturated conditions, as in (2). On Earth, it is known that a moist adiabat can be maintained even if the relative humidity is low almost everywhere in the atmosphere [K. A. Emanuel, J. D. Neelin, C. S. Bretherton, *Q. J. R. Meteorol. Soc.* **120**, 1111 (1994); K. M. Xu and K. A. Emanuel, *Mon. Weather Rev.* **117**, 1471 (1989)]. Our use of the moist adiabat is a conservative choice from the standpoint of sur-

face warming. A totally dry planet would likely adjust to the dry adiabat, which is steeper and would yield slightly greater surface temperatures than the "dry" case we show.

21. Adding 10% in mass of 10- $\mu\text{m}$  water ice particles to the cloud of Fig. 2 [particle radius ( $r$ ) = 10  $\mu\text{m}$ ;  $\tau$  = 10] reduces the absorbed solar energy by 2  $\text{W m}^{-2}$  and the scattering radiative forcing by 1.5  $\text{W m}^{-2}$  but increases the absorption-emission forcing by 8.5  $\text{W m}^{-2}$ , resulting in a 1.5 K surface warming. However, the effect of the water ice particles depends on their temperature. A lower, thicker water cloud would slightly cool the surface.

22. C. P. McKay, *Origins Life Evol. Biosphere* **27**, 263 (1997).  
 23. J. F. Kasting, D. P. Whitmire, R. T. Reynolds, *Icarus* **101**, 108 (1993).  
 24. K. Cadeira and J. F. Kasting, *Nature* **359**, 226 (1992).  
 25. We thank J. Kasting for lending us his model and for helpful comments and suggestions; and J.-L. Dufréne, R. Fournier, C. McKay, and B. Weare for their advice. R.T.P. gratefully acknowledges the support of the John Simon Guggenheim Foundation and of NSF (grant ATM-9505190).

11 August 1997; accepted 6 October 1997

## Mechanism for the Green Glow of the Upper Ionosphere

Steven L. Guberman

The generation of the green line of atomic oxygen by dissociative recombination of  $\text{O}_2^+$  occurs by the capture of an electron into a repulsive state of  $\text{O}_2$  followed by dissociation along another state of a different electronic symmetry. The two states are coupled together by mixed symmetry Rydberg states. Quantum chemical calculations give a rate coefficient at room temperature of  $(0.39_{-0.19}^{+0.31}) \times 10^{-8}$  cubic centimeters per second. The quantum yield of excited oxygen is within the range deduced from ground, rocket, and satellite observations. The rate coefficients and yields are needed in models of the optical emission, chemistry, and energy balance of planetary ionospheres.

The dissociative recombination (DR) of  $\text{O}_2^+$  with an electron ( $e^-$ ),  $\text{O}_2^+ + e^- \rightarrow \text{O} + \text{O}$ , is an important process in the ionospheres of Mars (1), Venus (2), and Earth (3). At Mars, DR can provide sufficient energy to the product O atoms to allow them to escape the atmosphere (1). In combination with the escape of hydrogen atoms, DR has been proposed as one of several nonthermal mechanisms for the disappearance of water from the Martian surface (1). At Venus, the collision of H atoms with energetic O atoms produced by DR can result in the escape of H from the atmosphere (4). At all three planets, one of the product O atoms can be generated in the excited  $^1\text{S}$  state, which is the source of the green airglow (caused by the  $^1\text{S}$  to  $^1\text{D}$  transition at 5577 Å) near 300 km in the terrestrial atmosphere (3, 5–7). At Earth, numerous ground, rocket, and satellite studies have reported an ionospheric  $\text{O}(^1\text{S})$  quantum yield [that is, the number of  $\text{O}(^1\text{S})$  atoms produced for every two product atoms] from DR of between 0.01 and 0.23 (3, 5–7). On the other hand, theoretical calculations with the assumed mechanisms for DR have given  $\text{O}(^1\text{S})$  quantum yields from the lowest ion vibrational level of 0.0016 (8) and 0.0012 (9). These results have led to the suggestion that another process is generating  $\text{O}(^1\text{S})$  in the ionosphere, although none could be identified (10). The

DR mechanism for the generation of  $\text{O}(^1\text{S})$  in the ionosphere and in planetary atmospheres has remained unknown.

I have shown that there is only one dissociative  $\text{O}_2$  potential curve,  $^1\Sigma_u^+$ , that produces  $\text{O}(^1\text{S})$  from the low vibrational levels of  $\text{O}_2^+$  (11). The  $^1\Sigma_u^+$  and ion potential curves (Fig. 1) cross between the  $v = 1$  and  $v = 2$  vibrational levels ( $v$  is the vibrational quantum number). The first calculation (8) of the rate coefficient included only the direct (12) recombination mechanism (Fig. 1), in which the electron is captured into the repulsive state without populating any intermediate states. Once captured, the electron can be emitted (autoionization), or the molecule can dissociate along the repulsive potential. The direct cross section and rate constant are approximately proportional to the square of the overlap between the continuum vibrational function for the  $^1\Sigma_u^+$  repulsive channel and the bound ion vibrational wave function. For  $v = 0$ , direct capture into  $^1\Sigma_u^+$  at low electron energies (for example,  $\epsilon$  in Fig. 1) occurs in the nonclassical region, where this overlap is small. The calculated quantum yield for  $\text{O}(^1\text{S})$  was 0.0016. Later calculations (9) included the indirect (13) recombination mechanism (Fig. 1). In indirect recombination,  $\text{O}_2^+ + e^- \rightarrow \text{O}_2(\text{RYD}) \rightarrow \text{O} + \text{O}$ , intermediate neutral Rydberg (RYD) states are populated that are predisassociated by the same dissociative state used in the direct mechanism. These calculations gave a quantum yield for  $\text{O}(^1\text{S})$  of

0.0012, which is smaller than the earlier results because of destructive interference between direct and indirect recombination and an order of magnitude below the yields derived from atmospheric observations.

An assumption common to all previous calculations of the DR mechanism is that molecular dissociation occurs along the same repulsive potential involved in the initial electron capture in direct DR (Fig. 1). The interaction between states of different electronic symmetries has never been accounted for in the DR mechanism. Only five states in addition to  $^1\Sigma_u^+(^1\text{S} + ^1\text{D})$  can provide routes for DR from the low vibrational levels of the ion,  $^3\Pi_u(^3\text{P} + ^3\text{P})$ ,  $^1\Pi_u(^3\text{P} + ^3\text{P})$ ,  $^3\Sigma_u^-(^3\text{P} + ^1\text{D})$ ,  $^1\Delta_u(^1\text{D} + ^1\text{D})$ , and  $^1\Sigma_u^-(^3\text{P} + ^3\text{P})$  (where the states of the product atoms are shown in parentheses) (11). All of these curves, except  $^1\Sigma_u^-$  and  $^1\Pi_u$ , cross the ion potential curve between the turning points of the  $v = 0$  vibrational level and have more favorable initial capture probabilities than that of  $^1\Sigma_u^+$ , the only channel that yields  $\text{O}(^1\text{S})$ .

A small interaction usually neglected in these calculations is spin-orbit coupling, the interaction of the magnetic field

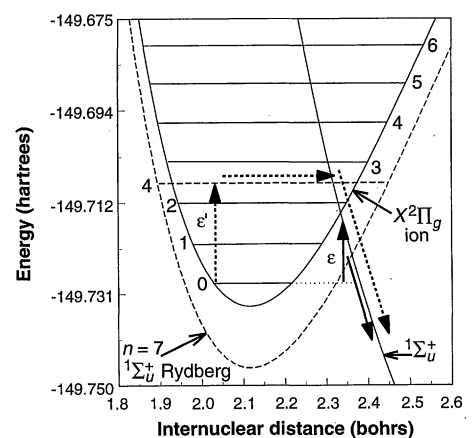


**Fig. 1.** Mechanisms of DR for dissociation along the  $^1\Sigma_u^+$  route. Direct recombination is shown by the solid arrows at electron energy  $\epsilon$ . Indirect recombination is shown by the dashed arrows at electron energy  $\epsilon'$ . Also shown are the  $v = 4$  vibrational level of the  $n = 7$   $^1\Sigma_u^+$  potential curve (dashed lines) and the lowest seven vibrational levels of the ion (solid lines).

Institute for Scientific Research, 33 Bedford Street, Lexington, MA 02173, USA. E-mail: slg@sci.org

due to an electron's orbital motion, with the magnetic field due to the electron's spin. The selection rules for spin-orbit coupling (14) allow states of  $^1\Sigma_u^+$  symmetry to couple to states of  $^3\Sigma_u^-$  and  $^3\Pi_u$  symmetry. Calculation of the spin-orbit matrix element between the Rydberg states of these symmetries shows that only the matrix element between the  $^3\Sigma_u^-$  and  $^1\Sigma_u^+$  Rydberg states is not negligible. In the multiconfiguration wave functions, both of these Rydberg states have an inner  $O_2^+$  core with an orbital occupancy that is dominated by  $1\sigma_g^2 1\sigma_u^2 2\sigma_g^2 2\sigma_u^2 3\sigma_g^2 1\pi_u^4 1\pi_g$  and a diffuse  $n\pi_u$  Rydberg orbital. The spin-orbit interaction is primarily due to the inner valence  $\pi_g$  orbital. Because this orbital is mostly singly occupied, there is no equivalent orbital of opposite spin to cancel the spin-orbit interaction. Because the  $\pi_g$  orbital is in the  $O_2^+$  core, the interaction is constant along the Rydberg series. As the principal quantum number  $n$  increases along the  $^3\Sigma_u^-$  and  $^1\Sigma_u^+$  Rydberg series, the unperturbed levels with different electronic symmetry but the same  $n$  and  $\nu$  become closer in energy and are degenerate in the limit of  $n \rightarrow \infty$ . At this limit, the energy splitting of the perturbed Rydberg levels is identical to the energy splitting between the lower  $^2\Pi_{1/2g}$  and upper  $^2\Pi_{3/2g}$  spin-orbit split  $O_2^+$  ground state,  $200 \text{ cm}^{-1}$  (15). The spin-orbit interaction matrix element is therefore 1/2 of this value,  $100 \text{ cm}^{-1}$ .

My calculations show that for the  $\nu = 1$  levels, the  $n = 9$  states are the lowest  $n$  states above the  $\nu = 0$  level of the  $^2\Pi_{1/2g}$   $O_2^+$  ground state. The unperturbed  $n = 9$ ,  $\nu_s = 1$ ,  $^1\Sigma_u^+$  and  $^3\Sigma_u^-$  levels are separated by only  $12 \text{ cm}^{-1}$ . An interaction of  $100 \text{ cm}^{-1}$ , although small, will almost completely mix these Rydberg levels. The amount of mixing

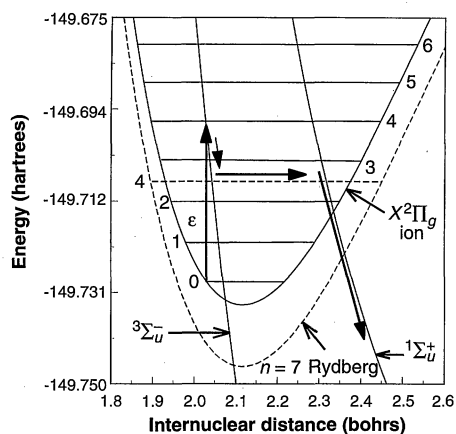


**Fig. 2.** The spin-orbit coupling mechanism for DR. Initial direct capture into the dissociative  $^3\Sigma_u^-$  state is shown by the vertical arrow at electron energy  $\epsilon$ . The Rydberg state (dashed lines) is of mixed  $^1\Sigma_u^+$  and  $^3\Sigma_u^-$  character. Final dissociation to  $O(^1S)$  occurs along the  $^1\Sigma_u^+$  channel.

varies with the energy spacing between Rydberg levels, that is, with  $n$ . The lowest amount of mixing occurs for  $n = 3$ , at which the unperturbed energy difference is  $572 \text{ cm}^{-1}$ . However, the  $n = 3$  levels play an important role because they have the highest predissociation coupling to the  $^3\Sigma_u^-$  and  $^1\Sigma_u^+$  dissociative valence states. Compared with the Rydberg-Rydberg state spin-orbit couplings, other spin-orbit couplings are smaller and have been neglected. These couplings include spin-orbit coupling between the dissociative states (small because of low vibrational overlap) and spin-orbit coupling between the dissociative and Rydberg states of the other electronic symmetry.

The spin-orbit mixing of Rydberg states results in the DR mechanism shown in Fig. 2. Initial direct electron capture is predominantly into the  $^3\Sigma_u^-$  state, which is coupled to mixed symmetry Rydberg levels. One example, namely the  $n = 7$ ,  $\nu = 4$  symmetry mixed level, is shown in Fig. 2. These mixed symmetry Rydberg levels are predissociated by both the  $^3\Sigma_u^-$  and  $^1\Sigma_u^+$  repulsive states. The flux exiting along the  $^1\Sigma_u^+$  channel produces  $O(^1S)$ . Thus, to generate  $O(^1S)$ , initial electron capture occurs mostly into a state that does not dissociate directly to  $O(^1S)$ .

I updated my previous calculations using larger  $[5s, 4p, 3d, 2f, 1g]$  basis sets (16). The orbitals were determined in complete active space multiconfiguration self-consistent field (17) calculations in which eight electrons were active and the  $1\sigma_g$ ,  $1\sigma_u$ ,  $2\sigma_g$ , and  $2\sigma_u$  orbitals were kept doubly occupied in all configurations. In the contracted, multireference configuration interaction wave functions (18), all single

and double excitations to the virtual orbitals were taken from a set of reference configurations in which 12 electrons (including those in the  $2\sigma$  orbitals) were active. The calculated and experimental spectroscopic constants agree well and indicate that the shapes of the calculated potential curves are accurate (19). All potential curve calculations were done with the MOLPRO programs (20).

The cross-section calculations were done with the multichannel quantum defect theory (MQDT) (9, 21) approach, revised to handle the spin-orbit coupling, multiple dissociative states, and the two ion core states. All vibrational wave functions were determined on a  $0.001a_0$  ( $1a_0 = 0.529177 \times 10^{-8} \text{ cm}$ ) grid between  $1.0 a_0$  and  $8.0 a_0$ . The cross sections were calculated on a  $0.0001\text{-eV}$  grid between  $0.0001$  and  $1.0 \text{ eV}$ . The electronic widths were calculated with high Rydberg orbitals (9). For the quantum defects, I used (for all  $n$ ) those appropriate to the  $n = 3$  Rydberg states (9). The MQDT calculations were done in the second order of the  $K$  (reaction) matrix. Nineteen vibrational levels were included in both the  $\Omega = 3/2$  and  $1/2$  ion core states. The  $40$  by  $40$   $K$  matrix included these 38 vibrational levels and the  $^3\Sigma_u^-$  and  $^1\Sigma_u^+$  dissociative states. Because the mixing caused by the spin-orbit interaction varies with  $n$ , a special approach was needed. The high vibrational levels ( $\nu \geq 10$ ) occur only once for  $n = 3$  within the region up to  $1.0 \text{ eV}$  above the  $\nu = 0$  levels. Therefore, the mixing for these important vibrational states was fixed at the  $n = 3$  value. The lower vibrational levels occur more than once for different  $n$  values below  $1.0 \text{ eV}$ . To account for the  $n$ -dependent mixing for these vibrational levels, I repeated the calculations for mixings corresponding to  $n = 4, 5, 6, 7, 8$ , and  $9$ , while keeping the  $\nu \geq 10$  levels at the  $n = 3$  mixing in each case. These calculations were also done with potential curves at the calculated and experimental excitation energies. The rate coefficients reported below are the average values over all these calculations.

The rate coefficients were determined from a Maxwellian average of the cross sections over the electron energy (Fig. 3). The spin-orbit coupling splits the ion ground state into  $^2\Pi_{1/2g}$  and  $^2\Pi_{3/2g}$  states, separated by only  $0.025 \text{ eV}$ . Nevertheless, the rate coefficients are quite different, especially at low electron temperature  $T_e$  because of the role of Rydberg resonances. At  $T_e = 300 \text{ K}$ , the calculated rate constant from  $\nu = 0$ ,  $^2\Pi_{1/2g}$  is  $(0.39^{+0.31}_{-0.19}) \times 10^{-8} \text{ cm}^3/\text{s}$ , and from  $\nu = 0$ ,  $^2\Pi_{3/2g}$ , the rate constant is  $(0.16^{+0.16}_{-0.13}) \times 10^{-8} \text{ cm}^3/\text{s}$ . For  $T_e = 800 \text{ K}$ , the  $\nu = 0$   $^2\Pi_{1/2g}$  and  $^2\Pi_{3/2g}$  rate constants are  $(0.31^{+0.03}_{-0.04}) \times 10^{-8}$  and

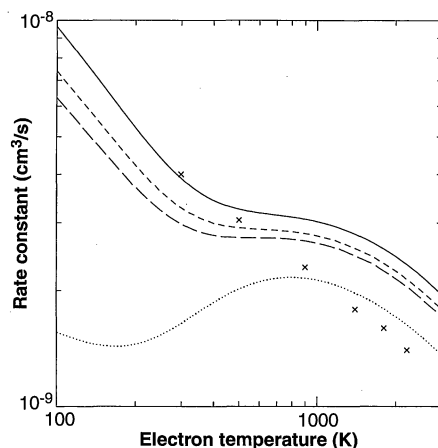


**Fig. 3.** Calculated rate coefficients for DR that produces  $O(^1S)$  from the  $\nu = 0$  level of  $O_2^+$   $X^2\Pi_{1/2g}$  (solid line), from  $\nu = 0$   $^2\Pi_{3/2g}$  (dotted line), for a Boltzmann vibrational temperature of  $300 \text{ K}$  (short-dashed line), and for an ionospheric temperature of  $800 \text{ K}$  (long-dashed line). The crosses show rate coefficients from (23).

$(0.22^{+0.14}_{-0.16}) \times 10^{-8}$  cm<sup>3</sup>/s, respectively. The plateau in the  ${}^2\Pi_{1/2g}$  rate and the peak in the  ${}^2\Pi_{3/2g}$  rate (Fig. 3) are caused by increasing Franck-Condon overlap between the  $v = 0$  wave function and the continuum vibrational wave function in the  ${}^1\Sigma_u^+$  dissociative channel as the electron energy increases. Dividing these rate constants by the total experimental DR rate constant (22) from  $v = 0$  of  $2.0 \times 10^{-7} \times (T_e/300)^{-0.65}$  cm<sup>3</sup>/s gives the quantum yields for O(<sup>1</sup>S). For  ${}^2\Pi_{1/2g}$ , these yields are  $0.020^{+0.015}_{-0.010}$  at  $T_e = 300$  K and  $0.029 \pm 0.003$  at  $T_e = 800$  K. For a 300 K ion temperature (including only the  ${}^2\Pi_{1/2g}$  and  ${}^2\Pi_{3/2g}$   $v = 0$  levels) and  $T_e = 300$  K, the quantum yield is  $0.016^{+0.013}_{-0.008}$ . At an 800 K ion temperature and  $T_e = 800$  K, the quantum yield is  $0.026^{+0.007}_{-0.008}$ .

The calculated yields at 800 K fall within the 0.01 to 0.23 range of yields derived from atmospheric measurements. The rate coefficients reported here are in good agreement with those derived from plasma spectroscopy measurements (23) (Fig. 3), in which the effective vibrational temperatures indicate that between 67 and 85% of the ions are in  $v = 0$  (24). Queffelec *et al.* (25) have reported a quantum yield for  $v = 0$  of 0.1 from a flowing afterglow experiment in which the O<sub>2</sub><sup>+</sup> ions were in  $v \leq 2$ . However, their experiment has high plasma densities (6) at which the recombination is dominated by processes other than two-body DR. A charge transfer experiment (26) that generates O<sub>2</sub> high Rydberg states and detects dissociation products gave a quantum yield for O(<sup>1</sup>S) from  $v = 0$  of 0.033, similar to the result reported here. A recent heavy-ion storage ring experiment (27) reported a quantum yield of  $0.05 \pm 0.02$ , also in agreement with my result.

## REFERENCES AND NOTES

1. M. B. McElroy, *Science* **175**, 443 (1972); J. L. Fox, *Geophys. Res. Lett.* **20**, 1747 (1993); M. H. G. Zhang, J. G. Luhmann, S. W. Bougher, A. F. Nagy, *J. Geophys. Res.* **98**, 10915 (1993).
2. J. L. Fox, *Adv. Space Res.* **10** (no. 5), 31 (1990); A. F. Nagy and T. E. Cravens, *Geophys. Res. Lett.* **15**, 433 (1988).
3. D. R. Bates, in *Applied Atomic Collision Physics*, vol. 1, H. S. W. Massey and D. R. Bates, Eds. (Academic Press, New York, 1982), pp. 149–224.
4. M. B. McElroy, M. J. Prather, J. M. Rodriguez, *Science* **215**, 1614 (1982).
5. J. E. Frederick *et al.*, *J. Geophys. Res.* **81**, 3923 (1976); P. B. Hays and W. E. Sharp, *ibid.* **78**, 1153 (1973); H. Takahashi *et al.*, *Planet. Space Sci.* **38**, 547 (1990).
6. D. R. Bates, *Planet. Space Sci.* **38**, 889 (1990).
7. V. J. Abreu, S. C. Solomon, W. E. Sharp, P. B. Hays, *J. Geophys. Res.* **88**, 4140 (1983).
8. S. L. Guberman, *Nature* **327**, 408 (1987).
9. \_\_\_\_\_ and A. Giusti-Suzor, *J. Chem. Phys.* **95**, 2602 (1991).
10. D. R. Bates, *Planet. Space Sci.* **40**, 893 (1992).
11. S. L. Guberman, in *Physics of Ion-Ion and Electron-Ion Collisions*, F. Brouillard and J. W. McGowan, Eds. (Plenum, New York, 1983), pp. 167–200.

12. D. R. Bates, *Phys. Rev.* **78**, 492 (1950).
13. J. N. Bardsley, *J. Phys. B* **1**, 365 (1968).
14. H. Lefebvre-Brion and R. W. Field, *Perturbations in the Spectra of Diatomic Molecules* (Academic Press, Orlando, FL, 1986).
15. The spin-orbit splitting used here was rounded off from the reported value of 200.33 cm<sup>-1</sup> for  $v = 0$ . See E. A. Colbourn and A. E. Douglas, *J. Mol. Spectrosc.* **65**, 332 (1977).
16. T. H. Dunning Jr., *J. Chem. Phys.* **90**, 1007 (1989).
17. H.-J. Werner and P. J. Knowles, *ibid.* **82**, 5053 (1985); P. J. Knowles and H.-J. Werner, *Chem. Phys. Lett.* **115**, 259 (1985).
18. H.-J. Werner and P. J. Knowles, *J. Chem. Phys.* **89**, 5803 (1988); P. J. Knowles and H.-J. Werner, *Chem. Phys. Lett.* **145**, 514 (1988).
19. For  ${}^3\Sigma_u^-$ , the differences between the calculated and experimental values (28) for the fundamental frequency, the equilibrium internuclear separation, and the excitation energy are 12 cm<sup>-1</sup>, 0.0006 a<sub>0</sub>, and 0.0642 eV, respectively. For  ${}^1\Sigma_u^+$  and O<sub>2</sub> + X<sup>2</sup> $\Pi_g$ , the excitation energy differences are 0.06 eV (29) and 0.1636 eV (28), respectively. These energy differences are accounted for in the rate coefficient uncertainties.
20. MOLPRO is a package of ab initio programs written by H.-J. Werner and P. J. Knowles, with contributions from J. Almlöf, R. D. Amos, M. J. O. Deegan, S. T. Elbert, C. Hampel, W. Meyer, K. Peterson, R. Pitzer, A. J. Stone, P. R. Taylor, and R. Lindh. Contact molpro-request@tc.bham.ac.uk
21. A. Giusti, *J. Phys. B* **13**, 3867 (1980).
22. P. Spanel, L. Dittrichova, D. Smith, *Int. J. Mass Spectrom. Ion Processes* **129**, 183 (1993).
23. E. C. Zipf, *Planet. Space Sci.* **36**, 621 (1988).
24. \_\_\_\_\_, *J. Geophys. Res.* **85**, 4232 (1980).
25. J. L. Queffelec, B. R. Rowe, F. Vallee, J. C. Gomet, M. Morlais, *J. Chem. Phys.* **91**, 5335 (1989).
26. H. Helm, I. Hazell, C. W. Walter, P. C. Cosby, in *Dissociative Recombination: Theory, Experiment, and Applications*, D. Zaffman, J. B. A. Mitchell, D. Schwalm, B. R. Rowe, Eds. (World Scientific, Singapore, 1996), pp. 139–150.
27. D. Kella, L. Vejby-Christensen, P. J. Johnson, H. B. Pedersen, L. H. Andersen, *Science* **276**, 1530 (1997); *ibid.* **277**, 167 (1997).
28. K. P. Huber and G. Herzberg, *Molecular Spectra and Molecular Structure, IV. Constants of Diatomic Molecules* (Van Nostrand Reinhold, New York, 1979); P. H. Kruper, *J. Phys. Chem. Ref. Data* **1**, 423 (1972).
29. B. R. Lewis *et al.*, *Phys. Rev. A* **52**, 2717 (1995).
30. Supported by NASA grants NAG5-4316 and NAG5-4286 and NSF grant ATM-9503224.

27 June 1997; accepted 7 October 1997

## Mantle Fluids in the San Andreas Fault System, California

B. M. Kennedy, Y. K. Kharaka, W. C. Evans, A. Ellwood, D. J. DePaolo, J. Thordsen, G. Ambats, R. H. Mariner

Fluids associated with the San Andreas and companion faults in central and south-central California have high <sup>3</sup>He/<sup>4</sup>He ratios. The lack of correlation between helium isotopes and fluid chemistry or local geology requires that fluids enter the fault system from the mantle. Mantle fluids passing through the ductile lower crust must enter the brittle fault zone at or near lithostatic pressures; estimates of fluid flux based on helium isotopes suggest that they may thus contribute directly to fault-weakening high-fluid pressures at seismogenic depths.

The San Andreas fault (SAF) is known to be a weak fault, and explanations for its weakness include either low-friction fault-zone materials or superhydrostatic fluid pressures within the fault zone (1–3). Abnormally high fluid pressures have been measured in pores at shallow crustal depths within the SAF system (4). For example, fluid pressure in the Varian–Phillips well, 1.4 km from the main trace of the SAF, is ~12 MPa over hydrostatic values at a depth of 1.5 km (5).

Models of fault weakening by elevated fluid pressures call on different fluid origins. Crustal fluids, connate or meteoric, may be

drawn into the fault zone in response to fault rupture and become trapped by mineral reactions; the high fluid pressures required to weaken the fault are reestablished by compaction of the sealed fault-zone materials (6–8). In this model, the base of the seismogenic zone, defined by the brittle-ductile transition, is treated as an impermeable boundary. In an alternative model, fault-weakening fluid pressures are generated by a high flux of deep crustal or mantle fluids that are continually supplied to the seismogenic zone from the ductile lower crust at superhydrostatic pressures (9).

To investigate fluid source and influence on SAF dynamics, we conducted a chemical and helium isotopic study of selected springs, seeps, and wells associated with the SAF and companion faults. Elevated discharge temperatures or salinity, unusual solute chemistry, high gas or water flow rates, or other indications of deep circulation or extensive water-rock interaction were used to select sampling sites. We found that the

B. M. Kennedy, Center for Isotope Geochemistry, Lawrence Berkeley National Laboratory, Berkeley, CA 94720, USA.

Y. K. Kharaka, W. C. Evans, J. Thordsen, G. Ambats, R. H. Mariner, Water Resources Division, U.S. Geological Survey, Menlo Park, CA 94025, USA.

A. Ellwood and D. J. DePaolo, Center for Isotope Geochemistry, Geology and Geophysics Department, University of California, and Lawrence Berkeley National Laboratory, Berkeley, CA 94720–4767, USA.